In situ investigation of mesoporous silicon oxidation kinetics using infrared emittance spectroscopy

Benjamin Bardet, Domingos de Sousa Meneses, Thomas Defforge, Jérôme Billoue, Gaël Gautier

PCCP

Accepted Manuscript

This article can be cited before page numbers have been issued, to do this please use: B. Bardet, D. De Sousa Meneses, T. Defforge, J. Billoué and G. Gautier, *Phys. Chem. Chem. Phys.*, 2016, DOI: 10.1039/C6CP02086K.

View Article Online
DOI: 10.1039/C6CP02086K

Journal Name

ARTICLE

In situ investigation of mesoporous silicon oxidation kinetics using infrared emittance spectroscopy

Received 00th January 20xx,
Accepted 00th January 20xx

DOI: 10.1039/x0xx00000x

www.rsc.org/

Benjamin Bardet,[a] Domingos De Sousa Meneses,[b] Thomas Defforge,[a] Jérôme Billoué,[a] Gaël Gautier[a*]

In this paper, we study the thermal oxidation kinetics of mesoporous silicon layers, synthesized by electrochemical anodization, from 260°C up to 1100°C. A specific apparatus is employed to heat the mesoporous samples in air and to record at the same time their infrared emittance. Based on Bruggeman effective medium approximation, an optical model is set up to realistically approximate the dielectric function of the porous material with an emphasis on the surface chemistry and oxide content. A transition temperature of 600°C is evidenced from data processing which gives evidence of two oxidation mechanisms with distinct kinetics. Between 260°C - 600°C, the oxidation is surface-limited with kinetics dependent on the hydrogen desorption rate. However, above 600°C, the oxide growth is limited by oxygen diffusion through the existing oxide layer. A parabolic law is employed to fit the oxidation rate and to extract the high-temperature activation energy (E_A=1.5 eV). A precise control of the oxide growth can thus be achieved.

Introduction

Mesoporous silicon (PS) is an attractive material owing to its highly-tunable nanostructure and its chemically modifiable surface.[1–3] Initially studied in the 70's to create deep silicon oxide wells for electronic applications,[4] oxidized PS is nowadays widely under investigation in the field of sensors,[5] lithium-ion batteries,[6–8] and drug delivery.[9–13] In the field of high-frequency electronics, oxidation of PS is expected to stabilize and enhance the semi-insulating properties of PS.[14–17] Good quality oxides can be formed at high-temperature though low-temperature oxidation can also be employed depending on the specifications of the application, *ie*. thermal budget, surface chemistry or oxidation level. A precise control of the stoichiometry of oxidized porous silicon (OPS) must be achieved.

In general, by comparing the initial state (before oxidation) and the final state (after oxidation), a quantification of the oxygen concentration in the structure can be assessed. The degree of oxidation in OPS layers can be characterized by various techniques, including weight measurements,[18] energy dispersive x-ray spectroscopy (EDX),[19,20] ellipsometry[21,22] and Fourier transform infrared spectroscopy.[23,24] In fact, oxidation temperature directly governs the surface chemistry and oxidation degree of PS which consequently tends to modify its properties.[20,25] In the early 80's, Unagami used the mass variation as a kinetics criteria to evaluate the degree of oxidation, but he did not take into account the transient state.[18] On another hand, Pap and coworkers quantified the relative change in oxidation degree at various temperatures by estimating the oxygen content using EDX.[19] However, using this method, only a rough estimation of activation energies was made depending on porosity. In the present study, an *in situ* characterization technique is developed to measure the emittance of PS while it is getting oxidized. The main benefit of this technique is the direct observation of the oxidation rate with temperature and time which allow us to analyze the kinetics of PS oxidation.

Experimental

PS formation

PS was obtained by anodization of a p-type (111) silicon wafer with a resistivity of 20-22 mΩ.cm. The anodization took place in a double-tank electrochemical cell filled with an aqueous electrolyte composed of 30 wt. % hydrofluoric acid and 25 wt. % acetic acid. The current density was fixed at 15 mA/cm² during 90 minutes. The sample was then thoroughly rinsed in deionized water and dried on a hot plate at 120°C. The resulting PS average thickness, measured by scanning electron microscopy (SEM), is 81 µm. The porosity was estimated at 30 % by weight measurements. Two additional PS layers with thicknesses of 20 µm and 50 µm and similar average porosity were also investigated to check the reliability of the

[a] Université François Rabelais de Tours, CNRS, CEA, INSA-CVL, GREMAN UMR 7347, Tours, France.
[b] CNRS, CEMHTI UPR3079, Université d'Orléans, F-45071 Orléans, France.
*Corresponding author: gael.gautier@univ-tours.fr

†Electronic Supplementary Information (ESI) available: The evolution of normal spectral emissivity (NSE) of samples with different thicknesses (20 µm and 50 µm) and their corresponding synthesis conditions are reported in Figure S1. The correlation between the experimental values and the fit of NSE is shown in Figure S2. The evolution of the dielectric function at different oxidation temperatures is compared with a silica reference in Figure S3. The extraction of *k* from the fit of $(\tau^*)^2$ is shown in Figure S4.
See DOI: 10.1039/x0xx00000x

characterization technique. The experimental etching conditions of these two samples are reported in Supplementary Information.

Emissivity apparatus

Measurement of PS emissivity requires a simultaneous acquisition of a reference flux (blackbody reference) and the sample flux. To address this purpose, a specific apparatus has been set up combining a CO_2 laser, a rotating turntable and two spectrometers. A detailed description of this characterization bench is given in a previous publication.[26]

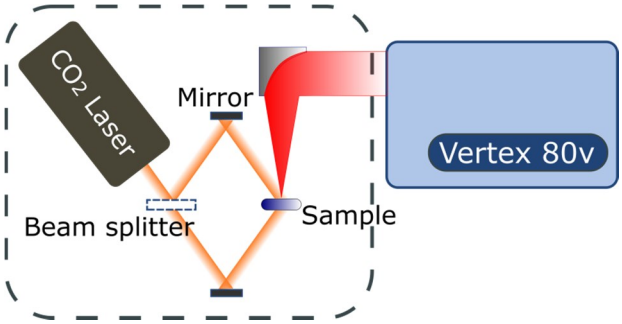

Figure 1 – Apparatus configuration for the measurement of the flux emitted by the PS sample.

Figure 1 is a schematic representation of the configuration of the emissivity measurement apparatus used to acquire the flux emitted by the PS wafer. The heating of the sample was adjusted by controlling the power of a (Coherent K500) CO_2 laser. In order to ensure temperature homogeneity inside the participating volume, the beam of the CO_2 laser is separated in two parts by a splitter to enable the heating of both sides of the sample at the same time. The selected spot on the PS sample is fixed by an aperture of 1 mm of diameter located inside the Bruker Vertex 80v spectrometer at an image point of the optical path. The whole system is placed within an enclosure that is continuously purged with dry air.

For a fixed laser power, the temperature of the sample is considered as constant (oscillations amplitude are less than 20°C). Therefore, the temperatures given in the next sections are average of the estimated values for a given laser power. Eight temperature plateaus from 260°C to 1100°C have been studied successively. Thus, the oxidation rate can be followed on the same sample and the first oxidation steps (T~300°C) stabilize the porous structure against pore coarsening.[27] For each temperature step, the duration was fixed to 100 minutes for low temperatures (T < 550°C) and 50 minutes for higher temperatures. To get high data density, measurements in the range 400-4000 cm^{-1} were acquired with a sampling rate of one scan per minute. The instrumental resolution was set to 4 cm^{-1}.

Temperature extraction and normalization of emissivity curves

The emitted flux is temperature-dependent and data need to be normalized. An accurate estimation of the temperature is thus required. Normalization is usually performed at Christiansen point, at which the material emittance is equal to one. In the case of PS, such a point does not exist. However, the relative flatness of emissivity between 2000 cm^{-1} and 4000 cm^{-1} was exploited as a criteria to extract the sample temperature with a relatively good accuracy. The gray body hypothesis enables to use the spectrometer as a bichromatic pyrometer to determine the sample temperature. The normal emittance spectra of PS were determined by correcting the samples fluxes, acquired on the sample and the blackbody reference, by the instrumental background flux and then by computing their ratio after a temperature correction of the sample flux using the Planck function.

Model development

The optical properties of OPS directly depend on the relative volumes of silicon, air, and silicon dioxide. To estimate its effective dielectric function (ε_e), a two stage application of the Bruggeman effective-medium-approximation (EMA) has been employed (1).[28] EMA is adapted to model mesoporous silicon in the infrared range because the dimensions of void and silicon are very small compared to the wavelength.[29,30]

$$f\frac{\varepsilon_e-\varepsilon_1}{2\varepsilon_e+\varepsilon_1}+(1-f)\frac{\varepsilon_e-\varepsilon_2}{2\varepsilon_e+\varepsilon_2}=0 \quad (1)$$

Where f is the volumetric fraction of silicon whose dielectric function is ε_1. ε_2 is computed in a first step using also EMA and represents the effective dielectric function of a mixed medium made of air and silicon dioxide with adequate contents. The optical response at room temperature of the doped silicon substrate was obtained by fitting its reflectance with a piecewise polynomial dielectric function model able to reproduce adequately the contribution of free carriers present in doped silicon.[31] The temperature dependence of the dielectric function of silicon dioxide has been acquired on a vitreous silica sample having less than 20 ppm of hydroxyl. The absorption bands induced by vibrational motions of Si-O bonds were taken into account by adding several causal Gaussian components to the dielectric function model.[32] Finally, the effective dielectric function model of OPS has been used with an optical model involving a thin film on a thick substrate to fit the emittance spectra.[33]

During oxidation, silicon and air volume decrease due to the oxide volume expansion. Indeed, correlations exist between the values of the three-phase ratio which are related to the oxidation mechanism. Considering the respective densities and atomic weights of Si and SiO_2, a simple calculation shows that a volumetric expansion of 2.27 occurs during the transformation of silicon into silicon oxide.[34,27,35] By means of spectroscopic ellipsometry in the infrared range, we recently demonstrated the validity of this assumption for similar mesoporous silicon samples.[36] As a result, the following relationships were added to constrain the model:

$$f_{Air}^{t}=f_{Air}^{t=0}-0.56\times f_{SiO_2}^{t} \quad (2)$$

$$f_{Si}^{t}=f_{Si}^{t=0}-0.44\times f_{SiO_2}^{t} \quad (3)$$

With $f_{Si}^{t}, f_{Air}^{t}, f_{SiO_2}^{t}$ corresponding respectively to volumetric fractions of silicon, air and silicon oxide at each instant t. $f_{Air}^{t=0}$ is fixed at 0.30 (initial porosity) and was measured before the experiment. The silicon dioxide content $f_{SiO_2}^{t}$ was quantified in respect with the intensity of its main absorption band

associated with vibrations of Si-O-Si around 1080 cm^{-1} at each instant *t*. However, the optical behavior of back-bonded oxide formed at low temperature differs from the silica reference. As a result, the modeling of the effective dielectric function of OPS was obtained by addition of the corresponding Gaussian profiles of the absorption peaks related to the surface chemistry of the material (see Table 1).

Results

Morphology of the porous silicon layer

The structure is composed of a PS layer on top of a monocrystalline silicon wafer. SEM images of the porous layer are shown in Figure 2. Due to the (111) orientation of the silicon substrate, pores are highly disoriented and the morphology is branched. The magnification is not high enough to estimate the pore size. Low-porosity mesoporous layers obtained from highly-doped p-type silicon wafers usually contain pores with a mean diameter of 4 to 10 nm.[1,37]

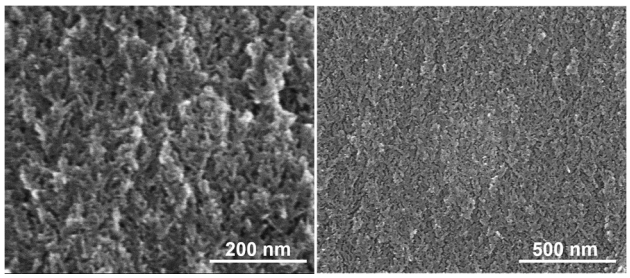

Figure 2 - SEM cross-section views of the PS layer at low magnification (left) and high magnification (right).

Evolution of PS surface chemistry with oxidation temperature

PS sample was *in situ* monitored during its oxidation in air. After a proper estimation of temperature, emissivity curves were normalized as previously described. Figure 3 is a superposition of normal spectral emissivity (NSE) of the 81 µm thick sample from 260°C to 1100°C after a constant heating period of 5 minutes (approximate duration needed for the heat to be homogeneously distributed).

Table 1 – Infrared band assignment taken from references.[38–42]

Wavenumber (cm^{-1})	Assignment
490	Si-O-Si rocking
800	Si-O-Si bending
1075	Si-O-Si stretching
1150	Si-O-Si stretching
2087	SiH stretching
2106	SiH_2 stretching
2139	SiH_3 stretching
2160	$OSiH_3$ stretching
2192	O_2SiH_2 stretching
2246	O_3SiH stretching
3500-3700	Si-OH stretching

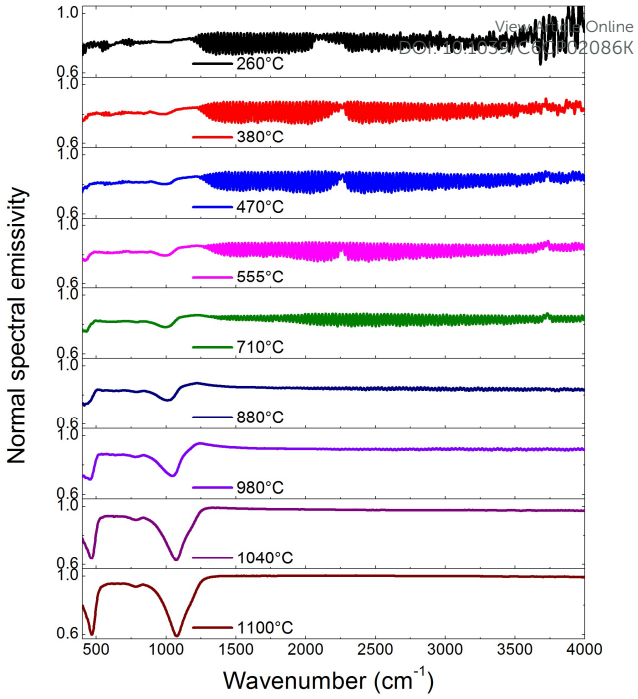

Figure 3 - Normal spectral emissivity evolution for the 81 µm-thick sample with temperature from 260°C to 1100°C after a heating duration of five minutes.

The monitoring measurement system was started at 260°C. As divergence occurred around 4000 cm^{-1}, it seems that is the minimal temperature at which emissivity curves can be studied with good accuracy. Table 1 summarizes the assignment of the different absorption peaks.

At low temperatures, oscillations also known as Fabry-Perot fringes[23], are present between 1500 cm^{-1} and 3500 cm^{-1} and completely vanish at temperatures close to 1000°C. These interference fringes are directly linked to the optical thickness of the porous layer, i.e. refractive index times sample thickness. Whenever possible, these fringes were used to approximate the emissivity curves. Between 2000 cm^{-1} and 2300 cm^{-1}, absorption peaks of hydrides species can be discerned from the attenuation of the interference fringes. These peaks are respectively related to silicon hydrides in the form of $Si\text{-}H_x$ and $O_y\text{-}Si\text{-}H_x$. A deconvolution of these peaks has been extensively done in the literature as it relates to the back-bond oxidation of PS (see Table 1 and Figure 4).[39,41,43,44] Finally, the evolution of oxidation is clearly distinguishable by the two prominent absorption peaks of silicon dioxide located around 490 cm^{-1} and 1080 cm^{-1} in Figure 3. The intensity of these peaks is specifically analyzed in the next section, as we focus on the determination of oxygen concentration in the structure.

View Article Online
DOI: 10.1039/C6CP02086K

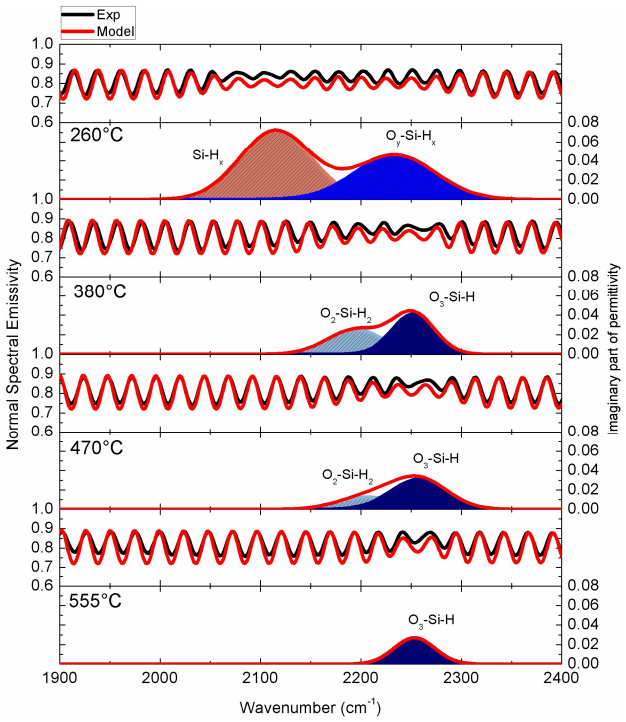

Figure 4 – Evolution of normal spectral emissivity and the imaginary part of permittivity extracted from the fitting procedure between 1900 cm^{-1} and 2400 cm^{-1}. Data are extracted after a heating duration of five minutes. The intensity of hydrides modes decreases due to hydrogen desorption.

A detailed analysis of the silicon hydrides evolution from 260°C to 555°C is shown in Figure 4. NSE evolution was fitted using EMA. Gaussian-shaped components are used to fit the silicon hydrides absorption peaks (see Table 1). At 260°C, hydrogen bonding is present in the form of Si-H_x, x=[1,3] and O_x-Si-H_{4-x}, x=[1,3].[45] A precise analysis of each specific mode cannot be done in the present study. The presence of oxygen is a sign of back-bond oxidation that occurs after the PS sample drying in air. When the temperature reaches 380°C, the peaks related to Si-H_x stretching modes shift to higher wavenumber. At this temperature, two peaks assigned to O_2-Si-H_2 (2192 cm^{-1}) and O_3-Si-H (2246 cm^{-1}) can be distinguished. From 380°C to 550°C, the peak related to O_2-Si-H_2 tends to disappear while the peak related to O_3-Si-H is still present. The latter also disappears when the temperature reaches 710°C. Finally, Si-OH bands are visible around 3600 cm^{-1} from 260°C to 710°C. However, a quantitative analysis of the silicon hydrides evolution with oxidation cannot be performed because of interference fringes. The consistency of these observations was verified on two additional samples with thicknesses of 20 µm and 50 µm respectively. The evolution of their respective normal spectral emissivity is plotted in Figure S1. The evolution of the oxidation peak intensity around 1080 cm^{-1} is very similar on the three samples. The amplitude of the Fabry Perot fringes is lower on the 81 µm-thick sample than on the thinner ones. Therefore, it was easier to distinguish the absorption peaks. A computational analysis of the peak intensity was thus more precise on the 81 µm-thick layer. As a result, this sample was specifically chosen to investigate the oxidation kinetics and discuss about the related mechanisms.

Refractive index of OPS

The normal spectral emissivity of the sample was fitted using a Bruggeman EMA according to the procedure described in the experimental section. This method was found to be very effective to approximate the dielectric function of PS at each oxidation stage. Figure S2 shows the good correlation between the experimental data and the fit. This procedure allows a precise determination of the dielectric function of the effective medium defined by its real part ε' and its imaginary part ε" according to equation (4).

$$\varepsilon = \varepsilon' + j\varepsilon" \quad (4)$$

With j the imaginary unit. The dielectric function of the sample tends to reach the one of the silica sample as it is shown in Figure S3. The imaginary part of the dielectric function (ε") being null at high wavenumber, the high frequency refractive index *n* can be extracted from ε' according to equation (5). The evolution of *n* with oxidation temperature is drawn in Figure 5. It was extracted from the 81 µm-thick sample. A similar evolution is observed for thinner PS layers. Uncertainties coming from the NSE normalization and the fitting procedure are estimated to be less than 5%.

$$\varepsilon' = n^2 \quad (5)$$

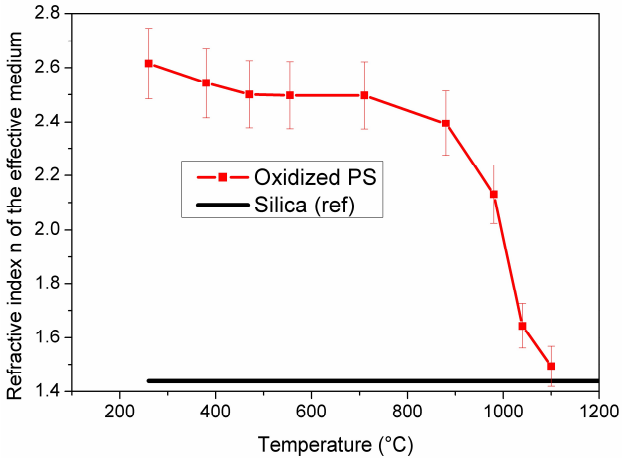

Figure 5 - Decrease of the refractive index *n* with oxidation. *n* is extracted from ε' at 4000 cm^{-1} (wavelength λ = 2.5 µm).

The refractive index is quite stable when the oxidation is performed between 260°C and 710°C. A strong decrease of *n* from 2.5 to 1.5 is observed at higher temperatures. At 1100°C, the refractive index of OPS is close to the one of the reference silica (*n* = 1.44) meaning that PS was almost fully oxidized.

Oxidation kinetics

A computational analysis of the silicon dioxide absorption peak allowed the determination of the silicon dioxide volumetric content at each instant *t*. To estimate the oxidation kinetics, the evolution of SiO_2 volumetric content is put in perspective with the oxidation time for different temperatures in Figure 6. Before laser heating, the structure already contains a small amount of silicon dioxide (~ 3%) due to room-temperature oxidation, also known as native oxide.[46] Starting at about 5%, the oxide content

reaches a maximum value of 94% at 1040°C. An increase of the temperature from 1040°C up to 1100°C did not increase the oxide content, meaning that silicon was almost totally consumed. For a constant CO_2 laser power, small variations of temperatures are observed. The maximum temperature disparity is found to be 35 °C for the 380°C plateau.

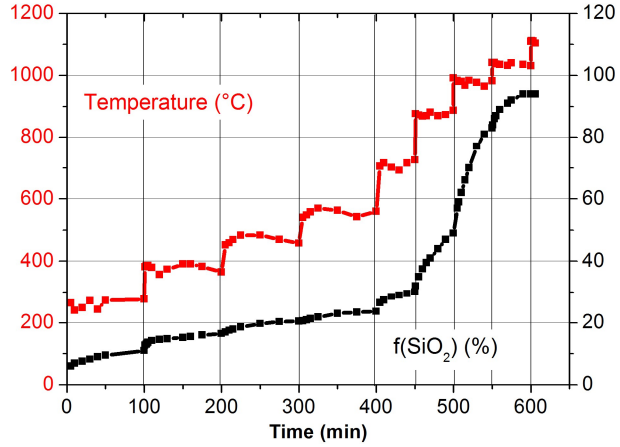

Figure 6 - Evolution of SiO_2 content with time and temperature from 260°C to 1100°C.

The evolution of the oxide content is not linear with temperature. At low temperatures, the rise of the oxide content is very slow. Oxidation becomes more intense beyond 700°C as we observe a rapid increase of the oxide content. In order to describe reaction kinetics, the oxidation degree τ is a convenient parameter defined as the ratio between consumed silicon and the initial silicon content (equation (6)).

$$\tau(t) = \frac{f_{Si}^{t=0} - f_{Si}^{t}}{f_{Si}^{t=0}} = \frac{0.44 \times f_{SiO_2}^{t}}{0.69} \qquad (6)$$

When the temperature is increased to the next stage, PS already contains certain amount of silicon dioxide and the silicon fraction of the structure is lower than if oxidation started on a fresh silicon surface. Therefore, another parameter, ie. τ^*, is introduced to take into account this cumulative phenomenon. The value of τ^* depends on both time and temperature and is defined in equation (7) as the volume of consumed silicon per volume of pre-existing silicon.

$$\tau^*(t,T) = \frac{0.44 \times \left(f_{SiO_2}^{t,T} - f_{SiO_2}^{t=0,T}\right)}{f_{Si}^{t=0,T}} \qquad (7)$$

The fraction $f_x^{t=0,T}$ is defined as the initial fraction of compound *x* (*x* being Si or SiO_2) when the temperature starts to increase to T. The evolution of τ^* with oxidation time is shown in Figure 7 for each temperature. For temperatures lower than 555°C, oxidation evolves at a relative slow rate (τ^*< 3%). Temperature does not have a significant impact on oxidation kinetics. Surprisingly, oxidation seems to be more intense at 380°C than at 470°C or 555°C. In the 710°C-980°C range, it is considerably heightened at each temperature plateau. However, at 1040°C, the increase of τ^* tends to slow down with time compared with the one at 980°C, presumably due to the full oxidation of the porous framework.

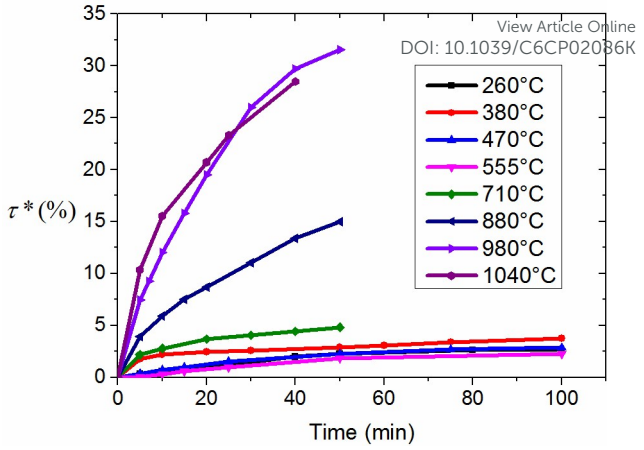

Figure 7 - Evolution of τ^* ratio as a function of time for each temperature step. The given temperature is an average of the estimated values for a given laser power.

Oxidation kinetics of monocrystalline silicon is well described by the Deal-Grove model[47] taking into account a linear-parabolic rate. Diffusion of oxygen from the surface to the interface is governed by a Fick's law. The relation between the oxide thickness *X* and time *t* is given by equation (8).

$$X^2 + AX = B(t + t_0) \qquad (8)$$

Where *A* and *B* are constants, ant t_0 accounts for the oxide already present at *t* = 0. The ratio *B/A* is called the linear rate constant and *B* is referred as the parabolic rate constant. Equation (8) can be reduced to a linear rate or a quadratic rate depending on the oxide thickness. For a thick film (*X*>>*A*), the model tends to a parabolic rate. We thus suggest the equation (9) to fit the evolution of τ^* with time. The corresponding fitted graphs are reported in Figure S4.

$$\tau^{*2} = k \times t \qquad (9)$$

With *k,* the parabolic rate constant. The evolution of *k* with temperature in an Arrhenius representation is shown in Figure 8.

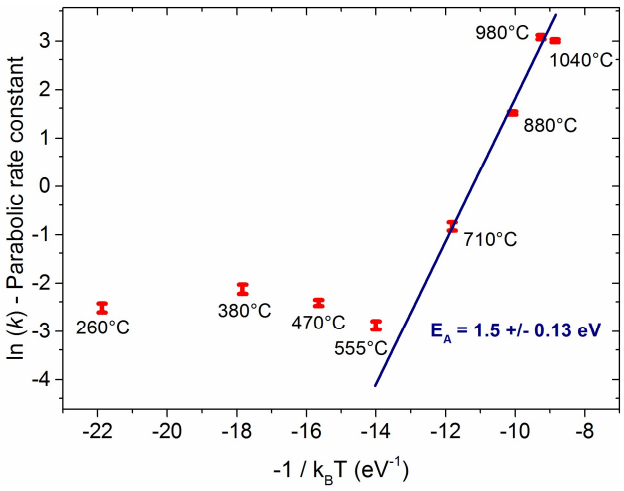

Figure 8 - Evolution of the natural logarithm of the parabolic rate constant *k* with -1/k_B.T (red symbol). k_B is the Boltzmann constant ($k_B = 8.62 \times 10^{-5}\, eV.K^{-1}$) and T is the

temperature. The blue line represents a linear regression of ln (*k*) in the high temperature range (710°C < T < 980°C).

Two distinct behaviors are highlighted with a transition temperature around 600°C. At low temperature (*i.e.* below 600°C), no obvious tendency is evidenced to correlate oxidation rate and temperature. The oxidation constant *k* is lower at 555°C than at 470°C. However, a significant increase of *k* is observed in the high temperature range. Between 710°C and 980°C, an activation energy of 1.5 eV was extracted from a linear fit (Figure 8). Beyond 980°C, the parabolic rate constant decreases. It is likely that the oxidation reaction becomes limited by the low quantity of remaining silicon to be oxidized.

Discussion

Oxidation of PS depends on physical and chemical mechanisms occurring at various temperatures. A transition temperature around 600°C is suggested in this part to discuss the different mechanisms affecting the oxidation kinetics.

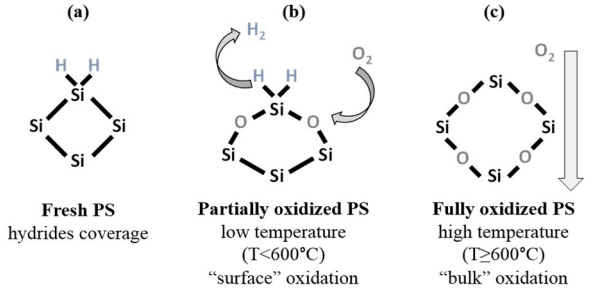

Figure 9 - Illustration of the incorporation of oxygen into PS structure depending on oxidation temperature. Two mechanisms are highlighted. Surface oxidation takes place at T<600°C with a back-bond oxidation and H_2 desorption (b). Bulk oxidation (oxygen diffusion in silica) prevails at T>600°C (c).

Low-temperature – a surface-limited reaction

Under 600°C, the temperature is too low to activate diffusion of oxygen through silicon dioxide. Thus, the oxidation is limited to the surface and occurs at a slow rate. At low temperature, it is well known that back-bond oxidation occurs due to the weaker Si-Si bond compared to Si-H bond.[48] A few oxide layers are expected to grow under the hydrogen passivated PS surface. A schematic of this passivation mechanism is illustrated in Figure 9b.

Once the first oxide layer is grown, the oxidation rate is limited by oxygen diffusion. However, the increase of temperature induces hydrogen desorption that tends to create new oxidation sites. This process is known to be thermally activated.[39,44,49] The desorption temperatures observed in this study (Figure 4) are in very good agreement with the literature: temperatures at which hydrogen desorbs lie in the range 200-600°C.[39,50,51] A first desorption step occurs around 200°C for hydrogen trapped in defects.[52] Desorption of hydrogen from Si-H_2 (O_2-Si-H_2) occurs in the range 340-420°C whereas it desorbs between 440°C and 590°C for Si-H (O_3-Si-H) depending on the initial oxidation state of the PS layer. Passivation of dangling bonds by oxygen follows hydrogen desorption. The relative decrease of *k* parameter (Figure 8) between 380°C and 555°C can thus be put in perspective with the decrease of the intensity of O_2-Si-H_2 modes observed in Figure 4. When temperature increases to 555°C, the density of available surface oxidation sites is thus lower than at 380°C. As a result, the model does not allow the extraction of activation energy in this temperature range. Moreover, it would be meaningless to extract a single value of activation energy between 260°C and 555°C because low-temperature oxidation is related to multiple desorption processes.

At these low temperatures, while surface oxidation is the main mechanism, the best way to expand the oxidation rate would be to increase the specific surface area of PS (while increasing the pore density together with decreasing the pore size).[52] For a PS sample containing very thin pore walls (less than a few nanometers) it seems realistic to achieve a complete oxidation in low-temperature annealing conditions. In this study, it is not applicable as the starting crystallite size is too large.

High-temperature oxidation – a diffusion-controlled process

Once hydrogen is totally desorbed, a SiO_x layer covers the entire surface of PS (Figure 9c). To thicken the oxide, oxygen must diffuse through the previously formed oxide. Diffusion mechanisms are known to be strongly activated by temperature. As a result, the oxide on pore walls grows at a higher rate when temperature is increased above 600°C. PS oxidation activation energy of 1.5 eV obtained in the present work is a bit larger than for the oxygen diffusion constant in vitreous silica (E_A = 1.17 eV)[53] or for the parabolic rate constant of planar "bulk" silicon dry oxidation from the Deal-Grove model (E_A = 1.24 eV)[47].Due to the decrease of pore diameter with oxidation,[45] the limited renewal of oxygen at the interface could also decrease the oxidation rate. However, the monotonic increase of *k* from 555°C to 980°C (Figure 8) implies that this effect is not predominant. In fact, oxidation of both PS and bulk monocrystalline silicon seems to occur in a very similar way at high temperature, *ie*. oxygen diffusion through silicon dioxide is the limiting mechanism. This work is somehow in discrepancy with previous characterizations of PS oxidation. Dealing with the oxidation of high porosity samples (70%-83%), activation energies in the range 0.46-0.57 eV were extracted by Pap *et al.* between 400°C and 800°C even though a linear tendency was not clearly evidenced.[19] Their activation energy was necessarily underestimated by the surface oxidation process occurring at T<600°C.

Finally, the influence of very high temperature annealing (T> 1000°C) on PS oxidation rate has not been clearly evidenced in the present study as the PS layer was almost fully oxidized beforehand. However, if the pore walls (i.e. silicon nano-crystallites) are sufficiently thick, it seems reasonable to expect an activation energy close to bulk silicon.

Conclusion

The kinetics of mesoporous silicon oxidation was investigated by means of infrared emittance spectroscopy. This technique

View Article Online
DOI: 10.1039/C6CP02856K

allows an *in situ* monitoring of the dielectric response of PS while it is getting oxidized in air with a CO_2 laser heating. This work covers a wide temperature range from 260°C to 1100°C. The dielectric function of PS with time was approximated using a three-phase Bruggeman EMA. The oxide volumetric content and the refractive index were put in perspective with temperature.

The oxidation rate was used as a parameter to quantify the oxidation kinetics. A transition temperature of 600°C was evidenced from this study. At low temperatures (T<600°C), oxidation is limited to the surface. Oxide growth occurs initially in a back-bonded form and then increases around 380°C due to the thermal desorption of hydrogen from SiH_2. An overall activation energy could not be extracted for low-temperature oxidation as it is a cumulative effect of distinct processes: back-bond oxidation and hydrogen desorption from silicon hydrides. To increase the oxide content, it was necessary to provide more energy by increasing the temperature beyond 600°C in order to activate the diffusion of oxygen through the oxide. From 710°C to 980°C, the activation energy for PS oxidation is close to the one of a thermally grown oxide on planar silicon suggesting that oxygen diffusion through the existing oxide layer is the limiting mechanism. As a result, oxidation kinetics of PS would be directly dependent on the size and the density of silicon crystallites rather than on the pore diameter.

Acknowledgments

The authors are very grateful to “Région Centre” for supporting the scientific project “PoreuxTherm” and to Tours 2015 supported by the french « Programme de l’économie numérique des Investissements d’Avenir ».

References

1 R. Herino, G. Bomchil, K. Barla, C. Bertrand and J. L. Ginoux, *J. Electrochem. Soc.*, 1987, **134**, 1994.
2 Michael J. Sailor, in *Handbook of Porous Silicon*, ed. L. Canham, Springer International Publishing, 2014, pp. 1–24.
3 T. Gao, J. Gao and M. J. Sailor, *Langmuir*, 2002, **18**, 9953–9957.
4 Y. Watanabe, Y. Arita, T. Yokoyama and Y. Igarashi, *J. Electrochem. Soc.*, 1975, **122**, 1351.
5 F. A. Harraz, *Sensors Actuators B Chem.*, 2014, **202**, 897–912.
6 F. Dai, R. Yi, M. L. Gordin, S. Chen and D. Wang, *RSC Adv.*, 2012, **2**, 12710.
7 Y. Chen, L. Liu, J. Xiong, T. Yang, Y. Qin and C. Yan, *Adv. Funct. Mater.*, 2015, **25**, 6701–6709.
8 J. Liang, X. Li, Z. Hou, W. Zhang, Y. Zhu and Y. Qian, *ACS Nano*, 2016, **10**, 2295–2304.
9 K. L. Jarvis, T. J. Barnes, A. Badalyan, P. Pendleton and C. A. Prestidge, *J. Phys. Chem. C*, 2008, **112**, 9717–9722.
10 M. Wang, P. S. Hartman, A. Loni, L. T. Canham, N. Bodiford and J. L. Coffer, *Langmuir*, 2015, **31**, 6179–6185.
11 M. A. Tölli, M. P. A. Ferreira, S. M. Kinnunen, J. Rysä, E. M. Mäkilä, Z. Szabó, R. E. Serpi, P. J. Ohukainen, M. J. Välimäki, A. M. R. Correia, J. J. Salonen, J. T. Hirvonen, H. J. Ruskoaho and H. A. Santos, *Biomaterials*, 2014, **35**, 8394–8405.
12 A. Tzur-Balter, Z. Shatsberg, M. Beckerman, E. Segal and N. Artzi, *Nat. Commun.*, 2015, **6**, 6208.
13 N. L. Fry, G. R. Boss and M. J. Sailor, *Chem. Mater.*, 2014, **26**, 2758–2764.
14 G. Gautier and P. Leduc, *Appl. Phys. Rev.*, 2014, **1**, 11101.
15 P. Sarafis, E. Hourdakis and A. G. Nassiopoulou, *Electron Devices, IEEE Trans.*, 2013, **60**, 1436–1443.
16 M. Capelle, J. Billoué, J. Concord, P. Poveda and G. Gautier, *Appl. Phys. Lett.*, 2014, **104**, 072104.
17 J.-Y. Y. Park and J.-H. H. Lee, *Mater. Chem. Phys.*, 2003, **82**, 134–139.
18 T. Unagami, *Jpn. J. Appl. Phys.*, 1980, **19**, 231–241.
19 A. E. Pap, K. Kordás, T. F. George and S. Leppävuori, *J. Phys. Chem. B*, 2004, **108**, 12744–12747.
20 G. Shtenberg, N. Massad-Ivanir, L. Fruk and E. Segal, *ACS Appl. Mater. Interfaces*, 2014, **6**, 16049–16055.
21 T. Lohner, M. Fried, P. Petrik, O. Polga, O. Polgár, J. Gyulai, W. Lehnert and O. Polgar, *Mater. Sci. Eng. B*, 2000, **69**, 182–187.
22 E. V Astrova and V. A. Tolmachev, *Mater. Sci. Eng. B*, 2000, **69**, 142–148.
23 S. a. Alekseev, V. Lysenko, V. N. Zaitsev and D. Barbier, *J. Phys. Chem. C*, 2007, **111**, 15217–15222.
24 M. J. Sailor, *Porous Silicon in Practice*, Wiley-VCH Verlag GmbH & Co. KGaA, Weinheim, Germany, 2011.
25 F. Moller, M. Ben Chorin, F. Koch and F. Mdler, *Thin Solid Films*, 1995, **255**, 16–19.
26 D. De Sousa Meneses, P. Melin, L. del Campo, L. Cosson and P. Echegut, *Infrared Phys. Technol.*, 2015, **69**, 96–101.
27 J. J. Yon, K. Barla, R. Herino and G. Bomchil, *J. Appl. Phys.*, 1987, **62**, 1042–1048.
28 D. Zhang, E. Cherkaev and M. P. Lamoureux, *Appl. Math. Comput.*, 2011, **217**, 7092–7107.
29 W. Theiss, *Surf. Sci. Rep.*, 1997, **29**, 91–192.
30 H. Sohn, in *Handbook of Porous Silicon*, Springer International Publishing, Cham, 2014, pp. 231–243.
31 D. De Sousa Meneses, B. Rousseau, P. Echegut and G. Matzen, *Appl. Spectrosc.*, 2007, **61**, 644–648.
32 D. De Sousa Meneses, M. Eckes, L. del Campo and P. Echegut, *J. Phys. Condens. Matter*, 2014, **26**, 255402.
33 W. Songprakob, R. Zallen, W. Liu and K. Bacher, *Phys. Rev. B*, 2000, **62**, 4501–4510.
34 K. Barla, G. Bomchil, R. Herino and G. Bomchil, *J. Appl. Phys.*, 1985, **59**, 439–441.
35 E. V Astrova, V. B. Voronkov, A. D. Remenyuk, V. B. Shuman and V. A. Tolmachev, *Semiconductors*, 1999, **33**, 1149–1155.
36 B. Fodor, E. Agocs, B. Bardet, T. Defforge, F. Cayrel, D. Alquier, M. Fried, G. Gautier and P. Petrik, *Microporous Mesoporous Mater.*, 2016, **227**, 112–120.
37 V. Lehmann, R. Stengl and a Luigart, *Mater. Sci. Eng. B*, 2000, **69**, 11–22.
38 J. Y. Ying, J. B. Benziger and A. Navrotsky, *J. Am. Ceram. Soc.*, 1993, **76**, 2571–2582.
39 P. Gupta, V. L. Colvin and S. M. George, *Phys. Rev. B*, 1988,

View Article Online
DOI: 10.1039/C6CP02086K

37, 8234.
40 Y. H. Ogata, T. Tsuboi, T. Sakka and S. Naito, *J. Porous Mater.*, 2000, **7**, 63–66.
41 Y. Ogata, *J. Electrochem. Soc.*, 1995, **142**, 195.
42 G. Lucovsky, *J. Vac. Sci. Technol. B Microelectron. Nanom. Struct.*, 1987, **5**, 530.
43 Y. Ogata, *J. Electrochem. Soc.*, 1995, **142**, 1595.
44 Y. J. Chabal, *Phys. Rev. B*, 1984, **29**, 3677–3680.
45 J. Riikonen, M. Salomäki, J. van Wonderen, M. Kemell, W. Xu, O. Korhonen, M. Ritala, F. MacMillan, J. Salonen and V.-P. Lehto, *Langmuir*, 2012, **28**, 10573–10583.
46 E. . Petrova, K. . Bogoslovskaya, L. . Balagurov and G. . Kochoradze, *Mater. Sci. Eng. B*, 2000, **69-70**, 152–156.
47 B. E. Deal and A. S. Grove, *J. Appl. Phys.*, 1965, **36**, 3770.
48 Y. Kato, T. Ito and A. Hiraki, *Appl. Surf. Sci.*, 1990, **41-42**, 614–618.
49 X. Zhang, Y. J. Chabal, S. B. Christman, E. E. Chaban and E. Garfunkel, *J. Vac. Sci. Technol. A Vacuum, Surfaces, Film.*, 2001, **19**, 1725.
50 A. Loni and L. T. Canham, *J. Appl. Phys.*, 2013, **113**, 173505.
51 J. Salonen, V.-P. Lehto and E. Laine, *Appl. Phys. Lett.*, 1997, **70**, 637.
52 V. Lysenko, F. Bidault, S. Alekseev, V. Zaitsev, D. Barbier, C. Turpin, F. Geobaldo, P. Rivolo and E. Garrone, *J. Phys. Chem. B*, 2005, **109**, 19711–19718.
53 F. J. Norton, *Nature*, 1961, **191**, 701–701.